

Efficient Density Control for 3D Gaussian Splatting

Xiaobin Deng Changyu Diao* Min Li Ruohan Yu Duanqing Xu*

Zhejiang University

{dengxiaobin, dcy, lmin, yuruohan, xdq}@zju.edu.cn



Figure 1. By improving adaptive density control of 3DGS [11], our EDC achieves superior rendering quality while using less Gaussians. Benefiting from Long-Axis Split, we successfully recover details of the ceiling lights and smoke detectors in the drjohnson [9] scene.

Abstract

3D Gaussian Splatting (3DGS) has demonstrated outstanding performance in novel view synthesis, achieving a balance between rendering quality and real-time performance. 3DGS employs Adaptive Density Control (ADC) to increase the number of Gaussians. However, the clone and split operations within ADC are not sufficiently efficient, impacting optimization speed and detail recovery. Additionally, overfitted Gaussians that affect rendering quality may exist, and the original ADC is unable to remove them. To address these issues, we propose two key innovations: (1) Long-Axis Split, which precisely controls the position, shape, and opacity of child Gaussians to minimize the difference before and after splitting. (2) Recovery-Aware Pruning, which leverages differences in recovery speed after resetting opacity to prune overfitted Gaussians, thereby improving generalization performance. Experimental results show that our method significantly enhances rendering quality. Code is available at <https://github.com/XiaoBin2001/EDC>.

1. Introduction

Novel view synthesis (NVS) is a classical problem in computer vision, with widespread applications in virtual reality, cultural heritage preservation, autonomous driving, and

other fields. Neural Radiance Field (NeRF) [19] introduced the use of neural networks to learn the structure and features of a scene, requiring only multi-view 2D images as training data to synthesize high-quality novel views. However, NeRF suffers from long synthesis times for individual views [7, 21], making real-time rendering challenging.

Recently, 3D Gaussian Splatting (3DGS) [11] has attracted attention due to its explicit representation and real-time rendering performance. 3DGS represents a scene using a large number of 3D Gaussian ellipsoids. The properties of these Gaussians include position, size, shape, opacity, and color, all of which can be optimized through differentiable rendering. 3DGS generates an initial set of Gaussians from the sparse points obtained through Structure from Motion (SfM) [23], and subsequently refines the scene representation by increasing Gaussian density via adaptive density control.

The goal of 3DGS is to achieve high-quality rendering by finely fitting the scene using a large number of 3D Gaussian ellipsoids. Its training process can be divided into two parts: (1) Increasing the number of Gaussians through adaptive density control. (2) Optimizing the parameters of the Gaussians via backpropagation. Densification operations are interleaved within the optimization process. To improve optimization efficiency, we should minimize their negative impact as much as possible. However, the clone and split operations used in 3DGS fail to meet this requirement. The clone operation relies on parameter updates from the current

*Corresponding authors.

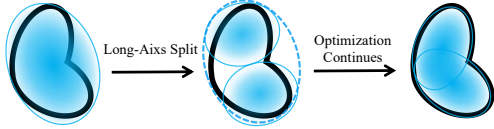


Figure 2. Our proposed Long-Axis Split can minimize the differences before and after splitting, thereby improving the optimization speed post-split.

iteration to separate it from its clone. However, this method does not always work effectively. Since two overlapping Gaussians may receive similar gradients, they cannot be individually optimized to fit the scene accurately. The split operation generates child’s coordinates using probabilistic sampling without altering the shape of the children, leading to a significant discrepancy between the overall shape distribution before and after splitting. Since the parent’s shape is optimized through backpropagation and closely aligns with the scene geometry, the shape changes introduced by splitting negatively impact the optimization process.

To minimize the adverse effects of densification operations, we propose Long-Axis Split (see Figure 2), a more precise alternative, to replace the original clone and split operations. Long-Axis Split adjusts the position, shape, opacity of the child Gaussians to minimize discrepancies before and after splitting while avoiding Gaussian overlaps. As Long-Axis Split reduces the negative impact of the densification process, it significantly improves the final rendering quality (see Figure 1). During the training process, we discover overfitted Gaussians that perform well in certain views but negatively impact rendering quality in other views. To mitigate the influence of those Gaussians, we propose Recovery-Aware Pruning, which leverages the difference in recovery rates between overfitted and normal Gaussians for pruning. The newly generated Gaussians contain both overfitted and normally fitted components. After multiple rounds of Recovery-Aware Pruning, the proportion of overfitted Gaussians among the remaining ones becomes significantly reduced, which notably improves generalization performance. On the challenging Mip-NeRF 360 dataset, EDC (TamingGS-Abs) achieves a notable improvement in PSNR from 27.48 to 28.15 compared to 3DGS, while also reducing the number of Gaussians from 3.3M to 2.1M.

Our contributions are summarized as follows:

- We propose Long-Axis Split, a more accurate densification operation, significantly enhancing reconstruction quality.
- We introduce Recovery-Aware Pruning, which eliminates overfitted Gaussians that harm generalization performance.
- Our method is plug-and-play and brings substantial improvements across multiple 3DGS variants.

2. Related Works

3D Gaussian Splatting (3DGS) [11] demonstrates outstanding performance in both rendering quality and speed, representing the current state-of-the-art in novel view synthesis. 3DGS has been widely adopted across fields including dynamic scenes [15, 27], simultaneous localization and mapping (SLAM) [10, 18, 28], 3D content generation [3, 25, 26, 31], autonomous driving [36], and high-fidelity human avatars [13, 16, 20, 24].

Numerous studies have focused on improving 3DGS rendering quality. For instance, Mip-Splatting [32] introduces a 3D smoothing filter and a 2D mipmap filter to eliminate aliasing artifacts present in 3DGS during scaling. To mitigate the impact of defocus blur on reconstruction quality, Deblurring 3DGS [14] applies a small multi-layer perceptron (MLP) to the covariance matrix, learning spatially varying blur effects. GaussianPro [4] leverages optimized depth and normal maps to guide densification, filling gaps in areas initialized via structure-from-motion (SfM) [23]. Spec-Gaussian [29] employs anisotropic spherical Gaussian appearance fields for Gaussian color modeling, enhancing 3DGS rendering quality in complex scenes with specular and anisotropic surfaces. Notably, all these enhancements rely on the original density control and could benefit from our proposed work.

3DGS increases Gaussians in a scene through a basic density control mechanism, yet the optimized scene still exhibits blurred regions that are challenging to refine merely by adding more Gaussians. MiniGS [6] addresses this by generating depth maps for trained scenes to reinitialize the sparse points, and identifies blurred Gaussians with large rendering areas during training, splitting them as needed. Pixel-GS [35] addresses blur by using the average gradient weighted by the pixel area covered by Gaussians in each view. AbsGS [30] and GOF [33] attribute blur in reconstructions to conflicts in gradient direction across pixels when computing Gaussian coordinate gradients. This conflict leads to larger Gaussians, which represent blur, receiving insufficient average gradients. To resolve this, they compute Gaussian coordinate gradients by taking the modulus of pixel coordinate gradients before summing. TamingGS [17] proposes a densification judgment condition that employs a weighted combination of multiple scores. The above studies propose improvements for initialization and densification criteria but do not address the densification operation itself. RevisingGS [22] optimizes the opacity bias of Gaussians after cloning. VCR-GauS [2] replaces the probabilistic sampling used in split operation with a method along the longest axis of the Gaussian, aiming to alleviate surface protrusions caused by the clustering of Gaussians after splitting. Although these improvements target the densification operation, they do not reduce the negative impact introduced by densification. We are the first to analyze the

adverse effects of densification operations and propose corresponding improvements.

There are also many optimization-based pruning methods. LightGaussian [5] calculates a global importance score for each Gaussian and prunes those with lower scores. EA-GLES [8] uses the average contribution of Gaussians to rendering across all views as the pruning criterion, where the rendering contribution is determined by opacity and rendering order. MiniGS [6] first optimizes the scene structure and then applies binary pruning to retain only the Gaussians that intersect with rays at their first hit point. Previous pruning methods have focused on significantly reducing the number of Gaussians to lower storage and rendering costs, whereas our Recovery-Aware Pruning focuses on mitigating the effects of overfitting.

3. Methods

3.1. Preliminaries

3DGS defines the scene as a set of anisotropic 3D Gaussian primitives:

$$G(x) = \exp\left(-\frac{1}{2}(x)^T \Sigma^{-1}(x)\right), \quad (1)$$

where Σ is the 3D covariance matrix and x represents the position relative to the Gaussian mean coordinates. To ensure the semi-definiteness of the covariance matrix, 3DGS reparameterizes it as a combination of a rotation matrix R and a scaling matrix S :

$$\Sigma = RSS^T R^T. \quad (2)$$

The scaling matrix S can be represented using a 3D vector s , while the rotation matrix R is obtained from the quaternion q . To render an image from a specified viewpoint, the color of each pixel p is obtained by blending N ordered Gaussians $\{G_i \mid i = 1, \dots, N\}$ that cover pixel p , with the following formula:

$$C = \sum_{i=1}^N c_i \alpha_i \prod_{j=1}^{i-1} (1 - \alpha_j), \quad (3)$$

where α_i is the value obtained by projecting G_i onto p and multiplying by the opacity of G_i , while c_i represents the color of G_i , expressed by SH coefficients.

3DGS initializes the scene using sparse points generated by SfM, and then increases the number and density of Gaussians in the scene through adaptive density control. Specifically, 3DGS calculates the cumulative average view-space positional gradients of Gaussians every 100 iterations, with each iteration training a single viewpoint. The formula for calculating the average gradient is as follows:

$$\frac{\sum_{k=1}^{M^i} \sqrt{\left(\frac{\partial L_k}{\partial \mu_{k,x}^i}\right)^2 + \left(\frac{\partial L_k}{\partial \mu_{k,y}^i}\right)^2}}{M^i} > \tau_{\text{pos}}, \quad (4)$$

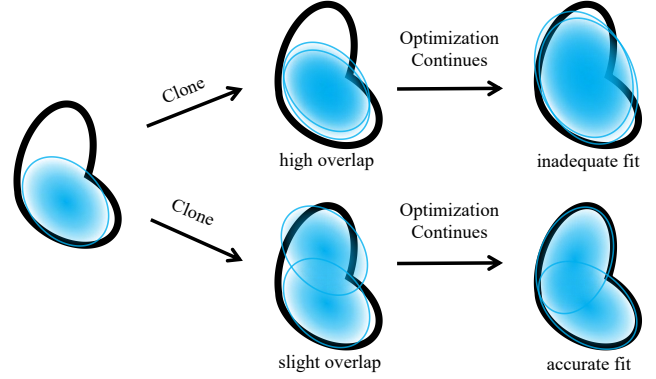


Figure 3. Compared to the normal case (below), two highly overlapping Gaussians after cloning (above) are more difficult to individually optimize for precise scene fitting.

where M^i represents the number of viewpoints in which the Gaussian participates during a cycle, τ_{pos} is the given densification threshold, $\frac{\partial L_k}{\partial \mu_{k,x}^i}$ and $\frac{\partial L_k}{\partial \mu_{k,y}^i}$ represent the gradients of the Gaussian with respect to the x and y for the current viewpoint, obtained by summing the gradients of each pixel with respect to the coordinates:

$$\frac{\partial L_k}{\partial \mu_{k,x}^i} = \sum_{j=1}^m \frac{\partial L_j}{\partial \mu_{i,x}}, \quad \frac{\partial L_k}{\partial \mu_{k,y}^i} = \sum_{j=1}^m \frac{\partial L_j}{\partial \mu_{i,y}}. \quad (5)$$

Gaussians with average gradients exceeding a predefined threshold undergo densification using either clone or split, depending on their size.

3.2. Analysis of Original ADC

Clone: Duplicate a small Gaussian with parameters (including position) identical to the parent. Since the clone operation occurs after the rendering step, the cloned Gaussian does not receive gradients during the current iteration. In subsequent parameter updates, only the parent Gaussian’s parameters are modified.

The degree of overlap between the two Gaussians after cloning depends on the magnitude of parameter changes of the parent Gaussian during the current iteration. However, not all Gaussians that require cloning exhibit large gradients during the iteration when cloning is performed. If the parameter update of the parent Gaussian is minimal in the current iteration, severe Gaussian overlap can occur. Due to receiving similar gradients, highly overlapping Gaussians struggle to be individually optimized in subsequent iterations to fit scene details (see Figure 3). Experimental analysis is provided in Section 4.7.

Split: A large Gaussian is replaced by two smaller Gaussians, which retain the same shape, opacity, and color as the original. Each smaller Gaussian is scaled down to 1/1.6 of the parent’s size. The coordinates of the two smaller Gaus-

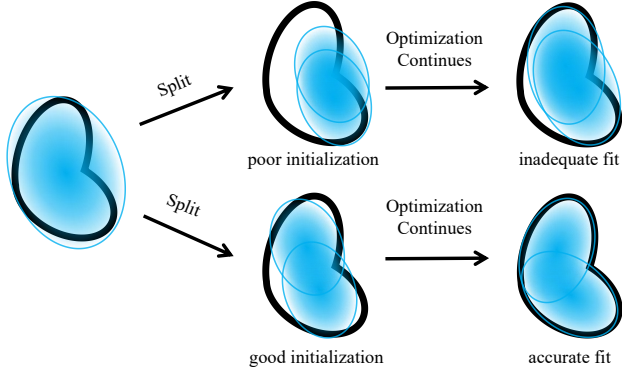


Figure 4. Split uses probabilistic sampling to generate the coordinates of child Gaussians. When the initial positions of the two child Gaussians are more reasonable (below), the final fitting result is better. Conversely, when the initial positions are less reasonable (above), the final fitting result is poorer.

sians are generated through Gaussian sampling, using the parent’s position and covariance matrix as parameters.

During training, the shapes of Gaussians gradually align with the target geometry, including over-reconstructed regions. Since the two smaller Gaussians maintain the same shape as the original Gaussian, their coverage cannot fully align with the parent’s shape, leading to deviations from the target geometry (see Figure 5). This geometric discrepancy slows down convergence during optimization and reduces the final rendering quality. Additionally, probabilistic sampling introduces extra uncertainty, resulting in greater fluctuations in training outcomes (see Figure 4).

Reset Opacity: During densification, an opacity reset operation is performed every 3000 iterations. Specifically, the opacity of Gaussians with opacity greater than 0.01 is reset to 0.01.

3DGS expects that resetting opacity in conjunction with pruning will help control the number of Gaussians and address floating artifacts. However, in practice, the combination of these operations has a negligible impact on the number of Gaussians and fails to eliminate floaters. Still, the process of resetting and subsequently restoring opacity repeatedly optimizes the contribution of different Gaussians in rendering, providing some improvement in reconstruction quality (see Section 4.7).

3.3. Long-axis Split

To better describe the differences between Long-Axis Split and the original split, we will present the explanation in three parts.

Position and Shape: If we consider a Gaussian as a point, the split operation is essentially performed along one dimension. Among the three axes of a Gaussian, we use its longest axis as the splitting dimension. The split Gaussians

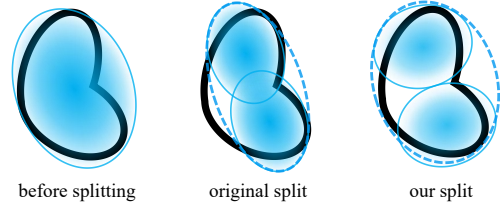


Figure 5. The original split method does not alter the shape of the sub-bodies, resulting in a shape formed by the child Gaussians that differs from the original shape of the parent Gaussian. In contrast, our method shortens the child Gaussians along their longest axis, ensuring that the shape of the covered region before and after the split remains approximately the same, thereby maximizing the densification efficiency.

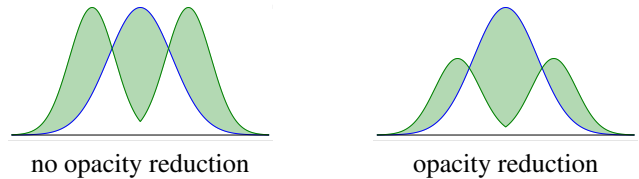


Figure 6. After splitting, the density of the corresponding region changes from a unimodal Gaussian distribution (blue curve) to a bimodal Gaussian distribution (green curve). If the opacity is not altered after the split (left), the change in the density distribution before and after the split is significant. By appropriately reducing the opacity of the split Gaussians (right), the variation in the density distribution can be reduced. The green shaded area represents the difference in density distribution before and after splitting.

are positioned symmetrically on both sides of the original Gaussian’s longest axis. To maximize the utilization of the shape information from the original Gaussian, we carefully adjust the shape of the child Gaussians to ensure that the overall shape remains consistent before and after splitting. Specifically, the radius along the longest axis of each child Gaussian is halved, while the radii along the other axes are shortened to 85% of their original values. This adjustment also helps mitigate the issue of excessively elongated Gaussians. Additionally, we set the spacing to the maximum radius of the original Gaussian to prevent overlap (see Figure 5).

Opacity: The split operation transforms the density distribution of the corresponding region from a single-center to a dual-center distribution (see Figure 6). To reduce the impact of density distribution changes before and after splitting, we lower the opacity of each child Gaussian to 60% of the original Gaussian. This also alleviates the opacity bias issue that arises when rendering rays sequentially pass through the two child Gaussians. This adjustment could improve the final rendering quality. Experimental results can be found in Section 4.5.

Split Only: 3DGS uses clone and split to address

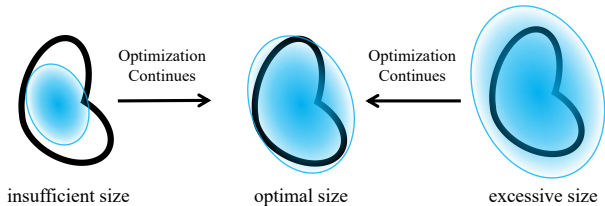


Figure 7. Through the process of backpropagation optimization, the parameters are driven to converge towards a single optimum point. Whether in cases of overfitting or underfitting, the sizes of the Gaussians tend to stabilize at a single consistent value.

under-reconstruction and over-reconstruction. However, during optimization, the size of Gaussians tends to converge to a value that balances under-reconstruction and over-reconstruction to minimize loss (see Figure 7). Therefore, we only use Long-Axis Split as the densification operation.

3.4. Recovery-Aware Pruning

3DGS may generate some overfitted Gaussians during the optimization process. These Gaussians contribute positively in some views but harm the rendering quality in other views. Overfitted Gaussians may have relatively high opacity, making it difficult to prune them directly using opacity-based methods.

Overfitted Gaussians provide positive contributions in some views and negative contributions in others, while normal Gaussians consistently contribute positively across all views. After resetting opacity, normal Gaussians will steadily increase their opacity until fully restored, whereas overfitted Gaussians experience fluctuations—opacity increases, decreases, and increases again—resulting in a significantly slower recovery. This difference in recovery speed can be leveraged for pruning.

The specific operation of Recovery-Aware Pruning involves pruning Gaussians with opacity less than 0.05 at the 300th iteration after resetting opacity, which occurs every 3000 iterations with a threshold of 0.01.

The Gaussians pruned by Recovery-Aware Pruning can be divided into two categories. The first category consists of redundant Gaussians whose opacity is inherently below 0.05, contributing minimally to rendering. Pruning these redundant Gaussians during densification reallocates resources to more impactful Gaussians, improving both training performance and generalization. The second category includes overfitted Gaussians that initially had opacity greater than 0.05. These Gaussians make significant contributions in some views, so they may reappear after being pruned. However, the newly generated Gaussians might no longer overfit. After multiple rounds of Recovery-Aware Pruning, the proportion of overfitted Gaussians is greatly re-

duced, significantly enhancing generalization performance.

While pruning redundant Gaussians improves rendering quality by reallocating resources to higher-contributing Gaussians, Recovery-Aware Pruning achieves its effect by correcting overfitted without altering resource allocation. A direct consequence is that Recovery-Aware Pruning enhances generalization performance without affecting training performance. Detailed experimental analysis can be found in Section 4.6.

The pruning threshold is only 0.05, with long intervals and execution limited to the densification phase. It does not strictly enforce that all Gaussians in the final result must have opacity greater than 0.05. In fact, pruning primarily reduces the number of Gaussians with opacity below 0.02, meaning its impact on rendering semi-transparent objects is limited.

4. Experiments

4.1. Datasets and metrics

We evaluated our method on real-world scenes from the Mip-NeRF 360 [1], Tanks and Temples [12], and Deep Blending [9] datasets. We selected all nine scenes from the Mip-NeRF 360 dataset, including five outdoor scenes and four indoor scenes. For the Tanks and Temples dataset, we chose the train and truck scenes, and for the Deep Blending dataset, we selected the drjohnson and playroom scenes. As with 3DGS, in each experiment, every 8th image was used as the validation set. We report peak signal-to-noise ratio (PSNR), structural similarity (SSIM), and perceptual metric (LPIPS) from [34] as quality evaluation metrics. All three scores were calculated using the methods provided by 3DGS.

4.2. Implementation

Our code is built upon the open-source 3DGS codebase. We evaluated the performance improvements of our method on 3DGS [11], TamingGS [17], and MiniGS [6]. TamingGS allows for setting an upper limit on the number of Gaussians, and by configuring different thresholds, we tested two versions: Small and Large. For the Large version, the Gaussian count upper limits were set to $3M$ for five outdoor scenes in the Mip-NeRF 360 dataset, $1.5M$ for drjohnson, and $1M$ for the remaining seven scenes. For the Small version, the thresholds were set to $1M$, $0.45M$, and $0.3M$, respectively.

We also tested the effect of TamingGS when using the gradient computation method proposed by AbsGS [30]. For the non-Abs version, all parameters remained consistent with the original implementation. For the Abs version, the splitting threshold was increased from 0.0002 to 0.0004, and the position learning rate combination was changed from 0.00016–0.0000016 to 0.0004–0.000002. Since EDC

| Dataset Method—Metric | Mip-NeRF360 | | | | | | Deep Blending | | | | | | Tanks&Temples | | | | | |
|--------------------------|--------------------------|--------------------------|---------------------------|-------|-------|-------|--------------------------|--------------------------|---------------------------|-------|-------|--------|--------------------------|--------------------------|---------------------------|-------|-------|--------|
| | <i>SSIM</i> [†] | <i>PSNR</i> [†] | <i>LPIPS</i> [‡] | Num/K | Train | FPS | <i>SSIM</i> [†] | <i>PSNR</i> [†] | <i>LPIPS</i> [‡] | Num/K | Train | FPS | <i>SSIM</i> [†] | <i>PSNR</i> [†] | <i>LPIPS</i> [‡] | Num/K | Train | FPS |
| 3DGS | 0.815 | 27.48 | 0.216 | 3338 | 21.4 | 169.0 | 0.904 | 29.57 | 0.244 | 2832 | 19.9 | 176.9 | 0.848 | 23.69 | 0.177 | 1847 | 11.7 | 226.8 |
| EDC-3DGS | 0.815 | 27.52 | 0.221 | 2158 | 16.4 | 304.8 | 0.907 | 29.87 | 0.241 | 1470 | 14.1 | 433.5 | 0.849 | 23.82 | 0.181 | 1074 | 8.3 | 468.9 |
| MiniGS | 0.817 | 27.13 | 0.226 | 411 | 14.5 | 680.6 | 0.908 | 30.00 | 0.255 | 311 | 12.2 | 1073.4 | 0.835 | 23.30 | 0.205 | 190 | 7.5 | 1272.0 |
| MiniGS-LAS | 0.820 | 27.24 | 0.222 | 437 | 15.2 | 667.0 | 0.908 | 30.09 | 0.254 | 312 | 13.1 | 1051.7 | 0.836 | 23.33 | 0.201 | 198 | 7.8 | 1236.3 |
| TamingGS-S | 0.801 | 27.42 | 0.253 | 689 | 5.3 | 300.3 | 0.904 | 29.90 | 0.264 | 375 | 3.9 | 433.5 | 0.836 | 23.93 | 0.213 | 300 | 3.1 | 504.0 |
| EDC-TamingGS-S | 0.808 | 27.59 | 0.244 | 689 | 4.8 | 400.7 | 0.907 | 30.00 | 0.255 | 375 | 3.5 | 542.1 | 0.846 | 24.18 | 0.199 | 300 | 2.9 | 626.0 |
| TamingGS-Abs-S | 0.803 | 27.20 | 0.240 | 689 | 6.0 | 250.9 | 0.906 | 29.84 | 0.262 | 375 | 4.8 | 295.1 | 0.837 | 23.77 | 0.210 | 300 | 3.4 | 421.4 |
| EDC-TamingGS-Abs-S | 0.823 | 27.72 | 0.216 | 689 | 5.4 | 328.1 | 0.911 | 30.14 | 0.247 | 375 | 4.2 | 458.7 | 0.854 | 24.24 | 0.188 | 300 | 3.0 | 596.2 |
| TamingGS-L | 0.820 | 27.89 | 0.215 | 2111 | 10.2 | 196.2 | 0.908 | 30.05 | 0.245 | 1250 | 6.9 | 310.9 | 0.856 | 24.32 | 0.176 | 1000 | 5.7 | 330.7 |
| EDC-TamingGS-L | 0.828 | 28.05 | 0.202 | 2111 | 9.5 | 267.2 | 0.909 | 30.12 | 0.236 | 1250 | 5.8 | 432.7 | 0.865 | 24.32 | 0.157 | 1000 | 5.4 | 429.8 |
| TamingGS-Abs-L | 0.825 | 27.88 | 0.197 | 2111 | 10.8 | 175.1 | 0.910 | 29.95 | 0.237 | 1250 | 7.7 | 234.5 | 0.862 | 24.13 | 0.164 | 1000 | 6.3 | 297.7 |
| EDC-TamingGS-Abs-L | 0.837 | 28.15 | 0.181 | 2111 | 9.9 | 236.4 | 0.913 | 30.10 | 0.226 | 1250 | 6.4 | 377.0 | 0.873 | 24.48 | 0.145 | 1000 | 5.4 | 391.3 |

Table 1. Quantitative results on the Mip-NeRF 360, Deep Blending, and Tanks and Temples datasets. Cells are highlighted as follows: best, and second best.

can significantly reduce the number of Gaussians under the same splitting threshold (see Section 4.3), this may result in some scenes failing to reach the upper limit set by TamingGS. For these scenes, we appropriately reduced the splitting threshold to meet the desired upper limit. Before the end of the warm-up phase (300th iteration), we performed an opacity pruning operation with a threshold of 0.02. This operation alleviates floaters caused by inconsistent lighting in certain scenes. All results were obtained after 30K training iterations.

As mentioned in Section 3.3, the other axes are shortened to 0.85 of their original lengths, and the opacity is reduced to 0.6 of its original value after splitting. As both values decrease from 1 to 0, the difference before and after splitting first decreases and then increases, causing the rendering quality to improve initially and degrade later. The values 0.85 and 0.6 were determined as extrema through testing, and in practice, variations within ± 0.05 yield similar results.

It is worth noting that for methods like MiniGS, which employs two large-scale depth-based initializations during densification and has a very high pruning ratio, both reset opacity and Recovery-Aware Pruning introduce negligible changes (MiniGS does not use reset opacity by default). Therefore, we only applied Long-Axis Split to MiniGS.

All experiments were conducted on a single 4090D GPU. All data presented are results we reproduced independently.

4.3. Quantitative Analysis

We selected 6 methods: 3DGS, MiniGS, TamingGS-S, TamingGS-L, TamingGS-Abs-S, and TamingGS-Abs-L to evaluate the improvements brought by EDC. As shown in Table 1, our method significantly enhances the quality of each benchmark. The PSNR scores for each scene can be found in Table 3 and Table 2.

EDC-TamingGS-Abs-L achieves the best rendering quality while using a significantly smaller number of Gaussians compared to 3DGS. Even under resource-constrained conditions, EDC-TamingGS-Abs-S achieves rendering quality that is notably superior to 3DGS. In the

| Dataset Method—Scene | Mip-NeRF360 | | | | | Tanks&Temples | |
|-------------------------|-------------|---------|--------|--------|----------|---------------|--------|
| | bicycle | flowers | garden | stump | treehill | train | truck |
| 3DGS | 25.213 | 21.539 | 27.361 | 26.539 | 22.495 | 21.958 | 25.414 |
| EDC-3DGS | 25.267 | 21.630 | 27.481 | 26.661 | 22.614 | 22.035 | 25.598 |
| MiniGS | 25.202 | 21.403 | 26.863 | 27.125 | 22.699 | 21.575 | 25.027 |
| MiniGS-LAS | 25.275 | 21.622 | 27.055 | 27.231 | 22.717 | 21.572 | 25.082 |
| TamingGS-S | 24.934 | 21.562 | 27.293 | 26.433 | 23.059 | 22.446 | 25.424 |
| EDC-TamingGS-S | 25.210 | 21.634 | 27.509 | 26.713 | 23.011 | 22.592 | 25.763 |
| TamingGS-Abs-S | 25.109 | 21.183 | 27.095 | 26.394 | 22.775 | 22.518 | 25.019 |
| EDC-TamingGS-Abs-S | 25.597 | 21.684 | 27.555 | 27.016 | 23.017 | 22.714 | 25.763 |
| TamingGS-L | 25.417 | 21.842 | 27.748 | 26.717 | 23.027 | 22.689 | 25.946 |
| EDC-TamingGS-L | 25.580 | 22.147 | 27.955 | 26.833 | 23.035 | 22.485 | 26.150 |
| TamingGS-Abs-L | 25.550 | 21.398 | 27.735 | 26.834 | 22.591 | 22.483 | 25.768 |
| EDC-TamingGS-Abs-L | 25.863 | 21.770 | 28.085 | 27.213 | 22.853 | 22.580 | 26.387 |

Table 2. PSNR scores for outdoor scenes from the Mip-NeRF 360 and Tanks and Temples datasets.

| Dataset Method—Scene | Mip-NeRF360 | | | | Deep Blending | |
|-------------------------|-------------|---------|---------|--------|---------------|----------|
| | bonsai | counter | kitchen | room | drjohnson | playroom |
| 3DGS | 32.242 | 29.016 | 31.474 | 31.446 | 29.119 | 30.019 |
| EDC-3DGS | 32.039 | 28.896 | 31.470 | 31.650 | 29.485 | 30.264 |
| MiniGS | 30.966 | 28.306 | 30.774 | 30.864 | 29.501 | 30.501 |
| MiniGS-LAS | 31.032 | 28.359 | 30.769 | 31.132 | 29.542 | 30.646 |
| TamingGS-S | 31.889 | 29.064 | 30.885 | 31.673 | 29.516 | 30.283 |
| EDC-TamingGS-S | 31.947 | 29.142 | 31.451 | 31.714 | 29.628 | 30.378 |
| TamingGS-Abs-S | 31.559 | 29.036 | 30.382 | 31.281 | 29.396 | 30.290 |
| EDC-TamingGS-Abs-S | 31.986 | 29.351 | 31.529 | 31.741 | 29.673 | 30.606 |
| TamingGS-L | 32.761 | 29.469 | 31.973 | 32.074 | 29.628 | 30.466 |
| EDC-TamingGS-L | 32.806 | 29.640 | 32.315 | 32.183 | 29.634 | 30.610 |
| TamingGS-Abs-L | 32.726 | 29.562 | 32.277 | 32.238 | 29.511 | 30.386 |
| EDC-TamingGS-Abs-L | 32.908 | 29.836 | 32.501 | 32.279 | 29.735 | 30.466 |

Table 3. PSNR scores for indoor scenes from the Mip-NeRF 360 and Deep Blending datasets.

following sections, we will analyze the results of each set of experiments.

3DGS: In EDC-3DGS, we maintained the same parameters as 3DGS, but the number of Gaussians differs substantially. One reason for this is that with Recovery-Aware Pruning, some regions undergo a process of pruning, regenerating, and re-pruning Gaussians, which impacts the densification speed. On the other hand, EDC achieves the same rendering quality with fewer Gaussians, meaning that under the same splitting threshold, the upper limit of Gaussians that EDC can achieve is lower. Even with fewer Gaussians, EDC still improves the rendering quality of 3DGS.

MiniGS: MiniGS employs two large-scale depth reinitializations, making its densification process no longer fully dependent on ADC. However, Long-Axis Split still en-

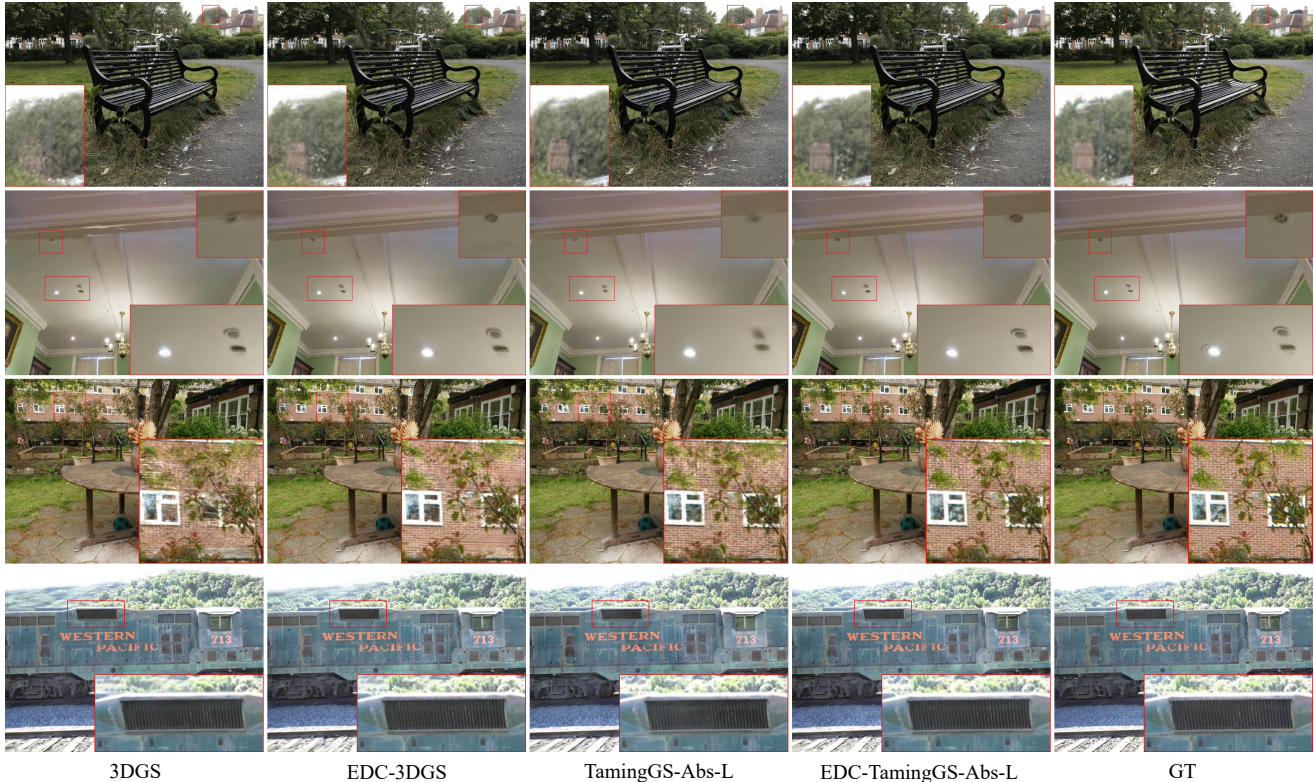


Figure 8. Qualitative analysis of the improvements brought by our approach across multiple scenes.

hances the rendering quality of MiniGS without introducing significant overhead. This demonstrates that our method can also be applied to compression-related tasks.

TamingGS: TamingGS previously achieved state-of-the-art performance in improving when to densify. Our tests show that incorporating the improvements proposed by AbsGS can further enhance the performance of TamingGS. Since TamingGS manually constrains the growth curve of Gaussian numbers, we are able to eliminate the influence of the number of Gaussians on the results and focus on analyzing the quality improvement brought by EDC.

In all four TamingGS experimental groups, our method brings significant quality improvements. Notably, EDC-TamingGS-Abs-L achieves a PSNR score of 28.15 on the Mip-NeRF 360 dataset. With the same number of Gaussians, our method also achieves over a 30% increase in rendering speed. This is because our method avoids overlapping Gaussians after splitting, reducing the average number of Gaussians traversed by rendering rays per pixel.

The peak number of Gaussians during the training of MiniGS is approximately ten times the final count, while for TamingGS, the peak equals the final count, indicating that TamingGS-S has a lower training requirements. After applying our method, only one-fifth of the training requirements is needed to achieve rendering quality surpassing 3DGS, which facilitates the wider adoption of 3DGS.

4.4. Qualitative Analysis

In Figure 8, we present the improvements of our method compared to 3DGS and TamingGS-Abs-L, with key areas magnified. Thanks to more precise splitting, our method is able to better recover details, such as the distant streetlights in the bicycle scene, the ceiling lights and smoke detectors in the drjohnson scene. Our method also performs better in regions with dense lines, such as the distant brick wall in the garden scene and the radiator in the train scene.

4.5. Ablation Experiments

We tested the impact of each improvement (including reduce the opacity of child Gaussians) on the Mip-NeRF 360 dataset (see Table 4). We also tested the results on two other datasets, but due to their higher variability, we only used Mip-NeRF 360 for the quantitative analysis to ensure experimental rigor. The baseline used for testing was TamingGS-Abs-S.

Long-Axis Split: When applying only Long-Axis Split, the average PSNR improved by 0.27. This demonstrates that Long-Axis Split is indeed more efficient than clone and split. Long-Axis Split minimizes the differences before and after splitting, leading to better fitting of details. As shown in Figure 9, when Long-Axis Split is not applied, the switch on the wall is barely reconstructed correctly. However, after



Figure 9. Qualitative comparison of two densification operations in the playroom scene, using TamingGS-Abs-S.

| Method—Metric | $SSIM^\dagger$ | $PSNR^\dagger$ | $LPIPS^\ddagger$ |
|-------------------------|----------------|----------------|------------------|
| Base | 0.803 | 27.20 | 0.240 |
| +Long-Axis Split | 0.812 | 24.47 | 0.233 |
| +Recovery-Aware Pruning | 0.812 | 27.41 | 0.227 |
| No opacity Reduction | 0.821 | 27.67 | 0.217 |
| Full | 0.823 | 27.72 | 0.216 |

Table 4. Results of the ablation study on the Mip-NeRF 360 dataset.

applying Long-Axis Split, the switch becomes clearly visible. Additionally, reducing opacity after splitting can also provide a certain performance boost.

Recovery-Aware Pruning: Applying only Recovery-Aware Pruning also leads to significant quality improvements. This is partly due to the elimination of redundancy and partly due to the mitigation of overfitting. Notably, when Long-Axis Split is used, Recovery-Aware Pruning can lead to even more substantial improvements in PSNR scores. Long-Axis Split uses a fixed splitting dimension, which reduces training fluctuations caused by probabilistic sampling but increases the likelihood of overfitting. Moreover, since Long-Axis Split has a stronger ability to fit detailed regions, these areas are more prone to overfitting. Recovery-Aware Pruning helps reduce the impact of overfitting and is highly complementary to Long-Axis Split. Therefore, we recommend applying both methods simultaneously in most cases.

4.6. Effectiveness of Recovery-Aware Pruning

The experimental setup in this subsection is based on TamingGS-Abs + Long-Axis Split/ TamingGS-Abs, with a Gaussian cap of $1M$ and the scene being bicycle.

We tested the results without pruning, pruning Gaussians with opacity less than 0.05 before resetting opacity (pruning redundant Gaussians), and using Recovery-Aware Pruning. The results are shown in Table 5. Firstly, pruning redundant Gaussians improves both training performance and generalization performance. Secondly, compared to pruning redundant Gaussians, Recovery-Aware Pruning significantly enhances generalization performance but does not notably improve training performance, consistent with the analysis

| Method—Metric | Test | Train | $o < 0.02$ | $o < 0.05$ | $o < 0.1$ |
|----------------|--------|--------|------------|------------|-----------|
| LAS-Base | 25.108 | 24.642 | 15.378 | 10.298 | 12.139 |
| LAS-Prune 0.05 | 25.190 | 24.788 | 3.809 | 5.836 | 14.201 |
| LAS-RAP | 25.294 | 24.811 | 0.910 | 4.737 | 13.181 |
| Base | 25.257 | 25.128 | 20.492 | 10.687 | 10.573 |
| Prune 0.05 | 25.420 | 25.373 | 5.267 | 6.367 | 14.243 |
| RAP | 25.597 | 25.368 | 0.971 | 4.166 | 11.893 |

Table 5. The analysis results of Recovery-Aware Pruning are presented as follows: the first three rows represent the results when using Long-Axis Split, and the last three rows represent the results when using Clone & Split. The testing scenario used was bicycle.

in Section 3.4. Pruning only drastically reduces the proportion of Gaussians with opacity less than 0.02, whose rendering contribution is minimal.

4.7. Analyze of Clone and Reset Opacity

In Section 3.2, we proposed that the clone operation relies on the current gradient to separate the cloned Gaussians. However, this method does not always work effectively. To visually demonstrate the impact of Gaussian overlap, we moved the cloned Gaussians along the major axis of the parent by $1/4$ of its axis length and compared the results with the original clone operation. The comparison was conducted using TamingGS-Abs, with a Gaussian cap of $1M$, and the scene being bicycle. The PSNR values for using clone + split, adjusted clone + split, and fully using split are 24.929, 24.989, and 25.047, respectively. Avoiding complete overlap between Gaussians improves rendering quality, however using only split achieved the best results.

We also conducted a simple test on the impact of resetting opacity itself using TamingGS-Abs-S + Long-Axis Split on the bicycle scene. The PSNR was 25.245 when using reset opacity and 25.206 when not using it. Additionally, reset opacity reduced the proportion of Gaussians with opacity greater than 0.9 from 0.12 to 0.03, with the excess allocation evenly distributed to Gaussians with opacity less than 0.5. This may suggest that a more balanced distribution of rendering contributions is beneficial for high-quality reconstruction.

5. Conclusion

3DGS employs Adaptive Density Control (ADC) to increase the number of Gaussians. The densification process is interleaved with optimization, and to improve efficiency, we should minimize the negative impact caused by densification. However, cloning and splitting operations fail to meet this requirement. To address this, we propose a more precise method called Long-Axis Splitting, which minimizes the differences before and after splitting. Additionally, our proposed Recovery-Aware Pruning successfully prunes overfitted Gaussians by leveraging the difference in recovery speed after resetting opacity. Overall, our method achieves state-of-the-art performance in rendering quality.

References

- [1] Jonathan T Barron, Ben Mildenhall, Dor Verbin, Pratul P Srinivasan, and Peter Hedman. Mip-nerf 360: Unbounded anti-aliased neural radiance fields. In *Proceedings of the IEEE/CVF conference on computer vision and pattern recognition*, pages 5470–5479, 2022. 5
- [2] Hanlin Chen, Fangyin Wei, Chen Li, Tianxin Huang, Yunsong Wang, and Gim Hee Lee. Vcr-gaus: View consistent depth-normal regularizer for gaussian surface reconstruction. *Advances in Neural Information Processing Systems*, 37: 139725–139750, 2024. 2
- [3] Zilong Chen, Feng Wang, Yikai Wang, and Huaping Liu. Text-to-3d using gaussian splatting. In *Proceedings of the IEEE/CVF Conference on Computer Vision and Pattern Recognition*, pages 21401–21412, 2024. 2
- [4] Kai Cheng, Xiaoxiao Long, Kaizhi Yang, Yao Yao, Wei Yin, Yuexin Ma, Wenping Wang, and Xuejin Chen. Gaussianpro: 3d gaussian splatting with progressive propagation. In *Forty-first International Conference on Machine Learning*, 2024. 2
- [5] Zhiwen Fan, Kevin Wang, Kairun Wen, Zehao Zhu, Dejia Xu, Zhangyang Wang, et al. Lightgaussian: Unbounded 3d gaussian compression with 15x reduction and 200+ fps. *Advances in neural information processing systems*, 37: 140138–140158, 2024. 3
- [6] Guangchi Fang and Bing Wang. Mini-splatting: Representing scenes with a constrained number of gaussians. *arXiv preprint arXiv:2403.14166*, 2024. 2, 3, 5
- [7] Sara Fridovich-Keil, Alex Yu, Matthew Tancik, Qinlong Chen, Benjamin Recht, and Angjoo Kanazawa. Plenoxels: Radiance fields without neural networks. In *Proceedings of the IEEE/CVF conference on computer vision and pattern recognition*, pages 5501–5510, 2022. 1
- [8] Sharath Girish, Kamal Gupta, and Abhinav Shrivastava. Eagles: Efficient accelerated 3d gaussians with lightweight encodings. In *European Conference on Computer Vision*, pages 54–71. Springer, 2024. 3
- [9] Peter Hedman, Julien Philip, True Price, Jan-Michael Frahm, George Drettakis, and Gabriel Brostow. Deep blending for free-viewpoint image-based rendering. *ACM Transactions on Graphics (TOG)*, 37(6):1–15, 2018. 1, 5
- [10] Nikhil Keetha, Jay Karhade, Krishna Murthy Jatavallabhula, Gengshan Yang, Sebastian Scherer, Deva Ramanan, and Jonathon Luiten. Splatam: Splat track & map 3d gaussians for dense rgb-d slam. In *Proceedings of the IEEE/CVF Conference on Computer Vision and Pattern Recognition*, pages 21357–21366, 2024. 2
- [11] Bernhard Kerbl, Georgios Kopanas, Thomas Leimkühler, and George Drettakis. 3d gaussian splatting for real-time radiance field rendering. *ACM Trans. Graph.*, 42(4):139–1, 2023. 1, 2, 5
- [12] Arno Knapitsch, Jaesik Park, Qian-Yi Zhou, and Vladlen Koltun. Tanks and temples: Benchmarking large-scale scene reconstruction. *ACM Transactions on Graphics (TOG)*, 36(4):1–13, 2017. 5
- [13] Muhammed Kocabas, Jen-Hao Rick Chang, James Gabriel, Oncel Tuzel, and Anurag Ranjan. Hugs: Human gaussian splats. In *Proceedings of the IEEE/CVF conference on computer vision and pattern recognition*, pages 505–515, 2024. 2
- [14] Byeonghyeon Lee, Howoong Lee, Xiangyu Sun, Usman Ali, and Eunbyung Park. Deblurring 3d gaussian splatting. *arXiv preprint arXiv:2401.00834*, 2024. 2
- [15] Youtian Lin, Zuozhuo Dai, Siyu Zhu, and Yao Yao. Gaussian-flow: 4d reconstruction with dynamic 3d gaussian particle. In *Proceedings of the IEEE/CVF Conference on Computer Vision and Pattern Recognition*, pages 21136–21145, 2024. 2
- [16] Xian Liu, Xiaohang Zhan, Jiayang Tang, Ying Shan, Gang Zeng, Dahua Lin, Xihui Liu, and Ziwei Liu. Humangaussian: Text-driven 3d human generation with gaussian splatting. In *Proceedings of the IEEE/CVF Conference on Computer Vision and Pattern Recognition*, pages 6646–6657, 2024. 2
- [17] Saswat Subhrajyoti Mallick, Rahul Goel, Bernhard Kerbl, Markus Steinberger, Francisco Vicente Carrasco, and Fernando De La Torre. Taming 3dgs: High-quality radiance fields with limited resources. In *SIGGRAPH Asia 2024 Conference Papers*, pages 1–11, 2024. 2, 5
- [18] Hidenobu Matsuki, Riku Murai, Paul HJ Kelly, and Andrew J Davison. Gaussian splatting slam. In *Proceedings of the IEEE/CVF Conference on Computer Vision and Pattern Recognition*, pages 18039–18048, 2024. 2
- [19] Ben Mildenhall, Pratul P Srinivasan, Matthew Tancik, Jonathan T Barron, Ravi Ramamoorthi, and Ren Ng. Nerf: Representing scenes as neural radiance fields for view synthesis. *Communications of the ACM*, 65(1):99–106, 2021. 1
- [20] Arthur Moreau, Jifei Song, Helisa Dharmo, Richard Shaw, Yiren Zhou, and Eduardo Pérez-Pellitero. Human gaussian splatting: Real-time rendering of animatable avatars. In *Proceedings of the IEEE/CVF Conference on Computer Vision and Pattern Recognition*, pages 788–798, 2024. 2
- [21] Thomas Müller, Alex Evans, Christoph Schied, and Alexander Keller. Instant neural graphics primitives with a multiresolution hash encoding. *ACM transactions on graphics (TOG)*, 41(4):1–15, 2022. 1
- [22] Samuel Rota Bulò, Lorenzo Porzi, and Peter Kotschieder. Revising densification in gaussian splatting. In *European Conference on Computer Vision*, pages 347–362. Springer, 2024. 2
- [23] Johannes L Schonberger and Jan-Michael Frahm. Structure-from-motion revisited. In *Proceedings of the IEEE conference on computer vision and pattern recognition*, pages 4104–4113, 2016. 1, 2
- [24] Zhijing Shao, Zhaolong Wang, Zhuang Li, Duotun Wang, Xiangru Lin, Yu Zhang, Mingming Fan, and Zeyu Wang. Splattingavatar: Realistic real-time human avatars with mesh-embedded gaussian splatting. In *Proceedings of the IEEE/CVF Conference on Computer Vision and Pattern Recognition*, pages 1606–1616, 2024. 2
- [25] Jiayang Tang, Jiawei Ren, Hang Zhou, Ziwei Liu, and Gang Zeng. Dreamgaussian: Generative gaussian splatting for efficient 3d content creation. *arXiv preprint arXiv:2309.16653*, 2023. 2

- [26] Alexander Vilesov, Pradyumna Chari, and Achuta Kadambi. Cg3d: Compositional generation for text-to-3d via gaussian splatting. *arXiv preprint arXiv:2311.17907*, 2023. [2](#)
- [27] Guanjun Wu, Taoran Yi, Jiemin Fang, Lingxi Xie, Xiaopeng Zhang, Wei Wei, Wenyu Liu, Qi Tian, and Xinggang Wang. 4d gaussian splatting for real-time dynamic scene rendering. In *Proceedings of the IEEE/CVF Conference on Computer Vision and Pattern Recognition*, pages 20310–20320, 2024. [2](#)
- [28] Chi Yan, Delin Qu, Dan Xu, Bin Zhao, Zhigang Wang, Dong Wang, and Xuelong Li. Gs-slam: Dense visual slam with 3d gaussian splatting. In *Proceedings of the IEEE/CVF Conference on Computer Vision and Pattern Recognition*, pages 19595–19604, 2024. [2](#)
- [29] Ziyi Yang, Xinyu Gao, Yangtian Sun, Yihua Huang, Xiaoyang Lyu, Wen Zhou, Shaohui Jiao, Xiaojuan Qi, and Xiaogang Jin. Spec-gaussian: Anisotropic view-dependent appearance for 3d gaussian splatting. *arXiv preprint arXiv:2402.15870*, 2024. [2](#)
- [30] Zongxin Ye, Wenyu Li, Sidun Liu, Peng Qiao, and Yong Dou. Absgs: Recovering fine details in 3d gaussian splatting. In *Proceedings of the 32nd ACM International Conference on Multimedia*, pages 1053–1061, 2024. [2](#), [5](#)
- [31] Taoran Yi, Jiemin Fang, Guanjun Wu, Lingxi Xie, Xiaopeng Zhang, Wenyu Liu, Qi Tian, and Xinggang Wang. Gaussian-dreamer: Fast generation from text to 3d gaussian splatting with point cloud priors. *arXiv preprint arXiv:2310.08529*, 2023. [2](#)
- [32] Zehao Yu, Anpei Chen, Binbin Huang, Torsten Sattler, and Andreas Geiger. Mip-splatting: Alias-free 3d gaussian splatting. In *Proceedings of the IEEE/CVF Conference on Computer Vision and Pattern Recognition*, pages 19447–19456, 2024. [2](#)
- [33] Zehao Yu, Torsten Sattler, and Andreas Geiger. Gaussian opacity fields: Efficient and compact surface reconstruction in unbounded scenes. *arXiv preprint arXiv:2404.10772*, 2024. [2](#)
- [34] Richard Zhang, Phillip Isola, Alexei A Efros, Eli Shechtman, and Oliver Wang. The unreasonable effectiveness of deep features as a perceptual metric. In *Proceedings of the IEEE conference on computer vision and pattern recognition*, pages 586–595, 2018. [5](#)
- [35] Zheng Zhang, Wenbo Hu, Yixing Lao, Tong He, and Hengshuang Zhao. Pixel-gs: Density control with pixel-aware gradient for 3d gaussian splatting. *arXiv preprint arXiv:2403.15530*, 2024. [2](#)
- [36] Xiaoyu Zhou, Zhiwei Lin, Xiaojun Shan, Yongtao Wang, Deqing Sun, and Ming-Hsuan Yang. Drivinggaussian: Composite gaussian splatting for surrounding dynamic autonomous driving scenes. In *Proceedings of the IEEE/CVF Conference on Computer Vision and Pattern Recognition*, pages 21634–21643, 2024. [2](#)